

The changing-type SN 2014C may come from an 11- M_{\odot} star stripped by binary interaction and violent eruption

Ning-Chen Sun[★], Justyn R. Maund and Paul A. Crowther

Department of Physics and Astronomy, University of Sheffield, Hicks Building, Hounsfield Road, Sheffield S3 7RH, UK

Accepted XXX. Received YYY; in original form ZZZ

ABSTRACT

SN 2014C was an unprecedented supernova (SN) that displayed a metamorphosis from Type Ib to Type IIn over ~ 200 days. This transformation is consistent with a helium star having exploded in a cavity surrounded by a dense shell of the progenitor’s stripped hydrogen envelope. For at least 5 years post-explosion, the ejecta continued to interact with an outer, extended component of circumstellar medium (CSM) that was ejected even before the dense shell. It is still unclear, however, what kind of progenitor could have undergone such a complicated mass-loss history before it produced this peculiar SN. In this paper, we report a new analysis of SN 2014C’s host star cluster based on data from the *Hubble Space Telescope* (*HST*). By carefully fitting its spectral energy distribution (SED), we derive a precise cluster age of $20.0^{+3.5}_{-2.6}$ Myr, which corresponds to the progenitor’s lifetime assuming coevolution. Combined with binary stellar evolution models, we find that SN 2014C’s progenitor may have been an $\sim 11-M_{\odot}$ star in a relatively wide binary system. The progenitor’s envelope was partially stripped by *Case C* or *Case BC* mass transfer via binary interaction, followed by a violent eruption that ejected the last hydrogen layer before terminal explosion. Thus, SN 2014C, in common with SNe 2006jc and 2015G, may be a third example that violent eruptions, with mass-loss rates matching luminous blue variable (LBV) giant eruptions, can also occur in much lower-mass massive stars if their envelopes are partially or completely stripped in interacting binaries.

Key words: supernovae: general – supernovae: individual: 2014C – stars: mass loss

1 INTRODUCTION

Massive stars experience a wide variety of mass loss during their lifetime, which can significantly affect their evolution and end fates (Smith 2014). Owing to their intense radiation, hot massive stars have much stronger line-driven winds than lower-mass stars (Bestenlehner, et al. 2014; Bestenlehner 2020). The stellar winds may become even stronger as they evolve into the red supergiant (RSG) stage, especially when their envelopes become dynamically unstable and develop large-amplitude pulsations (e.g. Yoon & Cantiello 2010). A subset of stars with initial masses $M_{\text{ini}} \geq 25 M_{\odot}$ may undergo a special phase as luminous blue variables (LBVs) with a high degree of mass loss (Vink 2012). LBVs are very unstable and exhibit irregular variabilities, the most pronounced of which is the so-called giant eruptions. During giant eruptions, LBVs increase their bolometric luminosities for months to years and suffer from extreme mass loss with mass-loss rates of $\dot{M} \gtrsim 10^{-2} M_{\odot} \text{ yr}^{-1}$ (e.g. the

Great Eruption of η Carina and P Cygni’s 1600 AD eruption; Humphreys, Davidson & Smith 1999; Smith & Hartigan 2006; Smith & Frew 2011). LBVs were believed to be a transitional phase from the main-sequence (MS) to the Wolf-Rayet (WR) stage (Conti 1976; Massey 2003). Accumulating evidence, however, shows that LBVs may have much more heterogeneous origins than previously thought (e.g. Smith, et al. 2019). Despite their importance, the diverse mass-loss processes are still a major uncertainty in understanding the evolution of massive stars.

SNe provide a unique opportunity to probe the mass loss of their progenitors at the latest evolutionary stages before core collapse. Many massive stars exhibit enhanced mass loss before their final explosion. For a subset of them, the pre-SN mass loss is so intense that the progenitors are surrounded by very dense CSM; after SN explosion, narrow/intermediate-width (10^2 – 10^3 km s^{-1}) emission lines can be produced as the SN ejecta catch up and collide with the dense CSM (Chugai, et al. 2004). SNe with such spectral features are classified as Type IIn (CSM is hydrogen-rich) or Type Ibn (CSM is hydrogen-poor and helium-rich; Pas-

[★] E-mail: n.sun@sheffield.ac.uk

pastorello, et al. 2008). Type IIn seems to be more heterogeneous than Type Ibn (Hosseinzadeh, et al. 2017), and some Type IIn SNe may arise from massive RSGs with superwinds (e.g. SNe 1998Z and 2005ip; Smith, et al. 2017). For many other Type IIn SNe, however, pre-SN mass-loss rates and CSM expansion velocities are consistent with those of LBV giant eruptions, suggesting that their progenitors may be massive LBVs (Smith 2017). While this is quite surprising, progenitor detections for a handful of Type IIn SNe confirms that LBVs can indeed directly undergo core collapse (e.g. SN 2005gl, Gal-Yam, et al. 2007, Gal-Yam & Leonard 2009; SN 2009ip, Mauerhan, et al. 2013). Coupled stellar evolution and atmospheric modelling also shows that some stars may exhibit LBV-like luminosity, spectra and chemical composition just before their final SN explosion (Groh, Meynet & Ekström 2013; Groh, et al. 2013).

For Type Ibn SNe, the pre-SN mass loss is also comparable to LBV giant eruptions in terms of their mass-loss rates and CSM expansion velocities (Smith 2017). For the class prototype SN 2006jc, a pre-SN outburst was even directly detected as an optical transient, with peak brightness and duration similar to those of LBV giant eruptions (Pastorello, et al. 2007). However, LBVs are still rich in hydrogen but Type Ibn SN progenitors are not. Early studies generally assumed that Type Ibn SNe arise from massive WR stars, which still have some residual instability after they descend from the LBV phase (e.g. Foley, et al. 2007; Pastorello, et al. 2008). On the other hand, the recent work of Shivvers, et al. 2017 and Sun, et al. 2020 (hereafter S20) rule out massive WR progenitors for the Type Ibn SNe 2006jc and 2015G and argue for much lower-mass progenitors stripped via binary interaction. This led S20 to conclude that violent pre-SN mass loss that resembles LBV giant eruptions can also occur in lower-mass massive stars ($8 < M_{\text{ini}} < 25 M_{\odot}$) if their envelopes are removed in interacting binary systems. Such a conclusion may confirm the theoretical prediction that envelope removal can aid the occurrence of pre-SN eruption since, without a massive envelope, the core convection-excited waves are easier to reach and trigger an outburst at the stellar surface (Fuller 2017; Fuller & Ro 2018).

SN 2014C is an unprecedented SN that exhibited a transformation from Type Ib to Type IIn (Milisavljevic, et al. 2015, hereafter M15). It had a very typical Type Ib spectrum soon after its explosion, suggesting that the progenitor was a stripped helium star with little remaining hydrogen. Over a timescale of 200 days, however, its spectrum started to show prominent H α emission with an intermediate width of 1000–2000 km s^{−1}. This indicates that the SN ejecta was interacting with a dense CSM shell, which was, however, rich in hydrogen. The interaction has also produced strong radio (Anderson, et al. 2017; Bietenholz, et al. 2018) and X-ray emission (Margutti, et al. 2017, hereafter M17). Detailed analysis shows that the shell is located at $\sim 6 \times 10^{16}$ cm from the progenitor and has a thickness of 10^{16} cm, a density of 2×10^6 cm^{−3} and a mass of $1.0\text{--}1.5 M_{\odot}$ (M17). The mass ejection that produced this shell had a mass-loss rate of $(3\text{--}5) \times 10^{-2} M_{\odot} \text{ yr}^{-1}$, assuming an ejection velocity of 100 km s^{−1} (M15). These characteristics are very similar to those of LBV giant eruptions. Thus, SN 2014C serves as another important laboratory to study the violent eruptions of stripped stars before their core collapse.

The dense shell is not the only CSM component

around SN 2014C’s progenitor. Tinyanont, et al. (2019, hereafter T19) carried out a long-term monitoring campaign of SN 2014C in the near- to mid-infrared wavelengths. They find that ejecta-CSM interaction was still on-going even at 5 years post-explosion. This suggests that there was an extended CSM component outside the dense shell out to at least $\sim 2 \times 10^{17}$ cm from the progenitor. This component has a different density profile from that of the dense shell and corresponds to a lower (but still very high) mass-loss rate of $(1.1\text{--}2.6) \times 10^{-3} M_{\odot} \text{ yr}^{-1}$. Thus, SN 2014C’s progenitor has experienced a very complicated mass-loss history. However, it is still unclear what kind of progenitor could form such a complex CSM configuration and produce SN 2014C with such a peculiar transformation from Type Ib to Type IIn.

M15 found SN 2014C to be spatially coincident with a star cluster, which very likely hosts the SN progenitor. Note that, perhaps quite surprisingly, core-collapse SNe rarely explode in bright star clusters (Smartt 2009); some of the progenitors may have been ejected from their host star clusters while some others may not be born in star clusters at all (recent studies show that massive stars form not only in compact clusters but also in much looser groups that are hierarchically structured; e.g. Sun, et al. 2017a,b, 2018). Thus, the host star cluster of SN 2014C (which we shall refer to as *Cluster A*) provides a precious opportunity to infer the properties and the pre-SN evolution of the SN progenitor. In particular, the age of *Cluster A* should correspond to the lifetime of the progenitor star, assuming they are coeval with each other. Following this idea, M15 derived an age of 30–300 Myr based on pre-explosion observations in the *B*, *V* and *R* bands with the ground-based *Subaru* telescope. M15 prefer a value at the lower range of potential ages given the strong H α emission detected in the *F658N* band by *HST*.

In this paper, we report a new analysis of SN 2014C’s host star cluster. We improve the age estimate in three aspects. First of all, we compile an *HST* dataset of SN 2014C over a much wider wavelength range from the UV to the near-infrared. The UV filters are very sensitive to the cluster age and thus can put much tighter constraints. Secondly, *Cluster A*, in the lower-resolution images, may be confused by the nearby sources in its close vicinity. The new data, with a much higher spatial resolution, allow us to resolve and remove the contamination of the nearby sources. Thirdly, we carry out a more detailed modelling of the cluster’s SED from not only its stellar population but also its gaseous nebula. The emission lines from the nebula can affect the brightness in the broad bands (e.g. H α in the *R* band) and can lead to systematic errors if they are not accounted for. On the other hand, the nebular lines serve as sensitive age indicators since they are powered by the ionising radiation from the massive stars. Our aim is to derive a precise estimate for *Cluster A*’s age, and in turn, to infer the property and the pre-SN evolution of SN 2014C’s progenitor.

Throughout this paper, we assume a distance of 14.7 ± 0.6 Mpc (Freedman, et al. 2001) and a solar metallicity for SN 2014C, both consistent with M15. This paper is structured as follows: Section 2 is a summary of the data used in this work. Section 3 describes how we measure the brightness of the host star cluster and in Section 4 we try to infer its properties. Section 5 further explores the properties and the pre-SN evolution of SN 2014C’s progenitor. We finally close this paper with a summary and discussion.

2 OBSERVATIONS

We used a series of *HST* observations of SN 2014C, a complete list of which is provided in Table 1. They were conducted by the *Wide Field and Planetary Camera 2* (*WFPC2*), *Wide Field Camera 3* (*WFC3*) *Ultraviolet-Visible* (*UVIS*) channel, and the *Advanced Camera for Surveys* (*ACS*) *Wide Field Channel* (*WFC*). The observations span a long period from five years before to more than five years post-explosion of SN 2014C and cover a long wavelength range from the UV to the *F814W* band. They also include observations in two narrow bands: the *WFPC2/F658N* band (Program 11966), which covers the $H\alpha$ $\lambda 6563$ and the $[N\ II]$ $\lambda 6584$ lines¹, and the *WFC3/F657N* band (Program 14202), which covers the $H\alpha$ $\lambda 6563$ and the $[N\ II]$ $\lambda\lambda 6548, 6584$ lines.

For the *WFPC2* observations (Program 11966), combined and well calibrated images were retrieved from the Hubble Legacy Archive² and used in this work without any further reduction. For the other observations, we retrieved the data from Mikulski Archive for Space Telescope³ and manually combined the dithered exposures for each filter with the *ASTRODRIZZLE* package⁴. In doing this, we set `drizz_cr_grow = 3` for more efficient removal of cosmic rays; all other drizzle parameters were kept unchanged as in the standard calibration pipeline (Lucas, et al. 2018; Genaro, et al. 2018).

3 PHOTOMETRY OF THE HOST STAR CLUSTER

Figure 1 shows the site of SN 2014C as imaged by *HST* in different filters and at different epochs. *Cluster A* is clearly revealed in all the images, and we derived its photometry by modelling all the sources in a $1.6'' \times 1.6''$ box region centred on it with the *GALFIT* package (Peng, et al. 2002, 2010). The details can be found in Appendix A. Note that, to the south and southwest of *Cluster A*, there are two additional sources (*S1* and *S2*, respectively) that are fainter but still visible in most of the images. *S1* and *S2* are associated with significant *WFC3/F657N* emission; in the *WFPC2/F658N* image, however, they are confused with and cannot be distinguished from *Cluster A* due to the poor spatial resolution (SN 2014C falls on the *WF3* chip of *WFPC2*, which has a pixel scale of $0.1''$). In Appendix B, we have estimated the contributions of *S1* and *S2* in the *WFPC2/F658N* band, which are comparable to the brightness of *Cluster A*. They are then removed from the measured brightness. The derived and decontaminated magnitudes (Vega magnitude system is used throughout this paper) of *Cluster A* are listed in Table 2 for all the *HST* observations.

The host galaxy of SN 2014C was also observed by the

8.2m *Subaru* Telescope with the *Suprime-Cam* instrument (Miyazaki, et al. 2002) before the explosion of SN 2014C. *Cluster A* is apparent in the *Subaru* images, and M15 derived its magnitudes with PSF photometry as $m_B = 22.18 \pm 0.13$, $m_V = 21.13 \pm 0.09$, and $m_R = 20.28 \pm 0.06$. We have independently performed data reduction and photometry on the *Subaru* images. Our results are consistent with those of M15 within errors. Strictly speaking, *Cluster A* is also confused with *S1*, *S2* and other nearby sources on the *Subaru* images. However, they are much fainter than *Cluster A* in the broad optical bands. Moreover, PSF photometry assigns lower weights to pixels that are far from the PSF centre. Thus, we do not perform any decontamination in the *B*-, *V*- and *R*-band photometry.

3.1 Was the SN still bright?

Apart from the *Subaru* observations and *HST* Program 11966, all other observations were acquired after the explosion of SN 2014C. Thus, it is very important to check whether the radiation from the SN itself was still significant. To this end, we compare the magnitudes of *Cluster A* at different epochs (Fig. 2), which may or may not be contaminated by SN 2014C. To aid the comparison, the *HST* native-filter magnitudes in the optical broad bands have been converted to the standard Johnson-Cousins system (*F438W* and *F475X* to the *B* band, *F555W* to the *V* band, and *F814W* to the *I* band) based on transformation relations reported by Sirianni, et al. (2005) and Harris (2018). The UV-band and narrow-band magnitudes are kept unchanged as in their native filters. In Fig. 2, we also show the late-time light curves of SN 2014C as observed by the 6.5m *MMT* telescope (M17), which have been transformed from the SDSS photometric system to the Johnson-Cousins system based on the relation of Jordi, Grebel & Ammon (2006). Note, however, that the transformation relations used here are calibrated based on normal stars; the presence of strong emission lines may lead to systematic uncertainties.

In the *B* and *V* bands, the late-time brightness was brighter than the pre-explosion level from $t = 586$ to 1462 days. This suggests that the radiation from SN 2014C was still significant in these bands. As SN 2014C experienced strong ejecta-CSM interaction, its late-time spectra exhibit prominent emission lines, the strongest of which include $H\alpha$ $\lambda 6563$, $H\beta$ $\lambda 4861$, $[O\ III]$ $\lambda 4363$ and $[O\ III]$ $\lambda\lambda 4959, 5007$, etc. (M15; Anderson, et al. 2017). The *B*-band magnitude converted from *F475X* at $t = 1096$ days is slightly brighter than that converted from *F438W* at $t = 586$ days. However, this does not necessarily suggest an increase in the SN's *B*-band brightness; this could also be due to the strong emission lines around $\sim 5000\ \text{\AA}$, which are covered by the extremely wide *F475X* band but not by the *F438W* band. The *V*-band (or the *F555W*-band) magnitude faded by 0.17 mag from $t = 1003$ to 1462 days, suggesting that the brightness of SN 2014C was on a decline. Thus, the late-time *HST* observations in the *F438W*, *F475X* and *F555W* bands are still subject to significant emission from the SN and cannot be directly used to infer the properties of the host star cluster.

In contrast, the *I*-band light curve remains almost constant from $t = 586$ to 1935 days (which corresponds to a time span of 3.7 years). The magnitude difference is only 0.08 mag, which is within the combined photometric er-

¹ Centred on $6591\ \text{\AA}$ and with a width of $28.5\ \text{\AA}$, the *WFPC2/F658N* filter can only cover the $[N\ II]$ $\lambda 6584$ line in the rest frame. Due to the recession velocity of *Cluster A* ($990\ \text{km s}^{-1}$; M15), however, this filter can also cover the $H\alpha$ $\lambda 6563$ line in the redshifted spectrum.

² <https://hla.stsci.edu>

³ <https://archive.stsci.edu>

⁴ <http://drizzlepac.stsci.edu>

Table 1. *HST* Observations of SN 2014C

Program ID	Date (UT)	Phase ^f (yr)	Instrument	Filter	Exposure Time (s)
11966 ^a	2009-01-01.2	-5.0	<i>WFPC2</i>	<i>F658N</i>	600.0
	2009-01-01.2	-5.0	<i>WFPC2</i>	<i>F658N</i>	600.0
	2009-01-01.2	-5.0	<i>WFPC2</i>	<i>F658N</i>	600.0
14202 ^b	2015-08-22.4	1.6	<i>WFC3/UVIS2</i>	<i>F438W</i>	1380.0
	2015-08-22.4	1.6	<i>WFC3/UVIS2</i>	<i>F814W</i>	1350.0
	2015-08-22.5	1.6	<i>WFC3/UVIS2</i>	<i>F275W</i>	1944.0
	2015-08-22.5	1.6	<i>WFC3/UVIS2</i>	<i>F657N</i>	1920.0
	2015-08-22.6	1.6	<i>WFC3/UVIS2</i>	<i>F657N</i>	480.0
14668 ^c	2016-10-12.1	2.7	<i>WFC3/UVIS</i>	<i>F336W</i>	780.0
	2016-10-12.1	2.7	<i>WFC3/UVIS</i>	<i>F555W</i>	710.0
14762 ^d	2017-01-13.3	3.0	<i>WFC3/UVIS2</i>	<i>F300X</i>	1200.0
	2017-01-13.3	3.0	<i>WFC3/UVIS2</i>	<i>F475X</i>	350.0
15166 ^e	2018-01-14.5	4.0	<i>WFC3/UVIS</i>	<i>F336W</i>	780.0
	2018-01-14.5	4.0	<i>WFC3/UVIS</i>	<i>F555W</i>	710.0
15645 ^e	2019-05-02.8	5.3	<i>ACS/WFC</i>	<i>F814W</i>	2152.0

PIs: (a) M. Regan; (b) D. Milisavljevic; (c) A. Filippenko; (d) J. R. Maund; (e) D. Sand.
(f): Phase is with respect to *V*-band maximum on 2014-01-13.

Table 2. Magnitudes of *Cluster A* from GALFIT results

Phase ^a (yr)	<i>F275W</i> (mag)	<i>F300X</i> (mag)	<i>F336W</i> (mag)	<i>F438W</i> (mag)	<i>F475X</i> (mag)	<i>F555W</i> (mag)	<i>F657N</i> (mag)	<i>F658N</i> (mag)	<i>F814W</i> (mag)
-5.0	19.54 (0.09)	...
1.6	21.72 (0.01)	21.58 (0.01)	18.13 (0.01)	...	19.67 (0.08)
2.7	21.40 (0.03)	20.51 (0.02)
3.0	...	21.97 (0.01)	20.76 (0.03)
4.0	21.46 (0.04)	20.68 (0.02)
5.3	19.59 (0.07)

(a): Phase is with respect to *V*-band maximum on 2014-01-13.

ror (0.11 mag). We also find that the *I*-band magnitude at $t = 586$ days is consistent with the extrapolation of SN 2014C's earlier *MMT* light curve. Thus, it is possible that SN 2014C has faded significantly in the *I* band by $t = 586$ days, after which the light from *Cluster A* dominates the *I*-band brightness. We also note that the emission lines in the *I* band are much weaker than those in the *B*, *V* and *R* bands (M15; Anderson, et al. 2017). To be conservative, however, we do not exclude the possibility that the SN was still bright in the *I* band and we regard the measured *F814W* brightness as an upper limit for *Cluster A*.

Similarly, the *F336W*-band magnitude also remains almost constant from $t = 1003$ to 1462 days (which corresponds to a time span of 1.3 years). The magnitude difference is only 0.06 mag, which is comparable to the combined photometric error (0.05 mag). Note that during the same period the *F555W*-band magnitudes faded by 0.17 mag. Yet, SN 2014C, like many other interacting SNe, exhibits a blue pseudo-continuum, which may arise from blended iron lines produced by ejecta-CSM interaction (M15; see also, e.g., SN 2006jc, Pastorello, et al. 2007; Bufano, et al. 2009). As a result, we cannot rule out the possibility that the *F336W* band is contaminated by the pseudo-continuum emission

from the SN. Thus, we regard the *F336W*-band brightness also as an upper limit for *Cluster A*.

The *F275W* and *F300X* bands were only observed at a single epoch. Both bands cover the [Mg II] doublets at ~ 2800 Å; the *F300X* band also covers the [Fe II] line at ~ 2950 Å. These two lines are important coolants and often appear to be very strong in emission for interacting SNe (Fesen, et al. 1999; Fransson, et al. 2005; Bufano, et al. 2009). Thus, *F275W* and *F300X* bands may be contaminated by the SN light, although it is difficult to estimate the amount of its contribution. Still, they place important upper limits for the brightness of *Cluster A* at UV wavelengths.

In summary, SN 2014C's light was still significant until at least 4 years post explosion (the last epoch of *F555W* observation). This is consistent with the conclusion of T19 that SN 2014C experiences on-going interaction between its ejecta and CSM at large distances. Still, the *HST* observations provide very important constraints on *Cluster A*'s SED from the UV to the *F814W* band, a much wider wavelength coverage than the pre-explosion observations in the *B*, *V*, *R* and *F658N* bands. Thanks to the higher spatial resolution provided by the new data, the measured SED of *Cluster A*

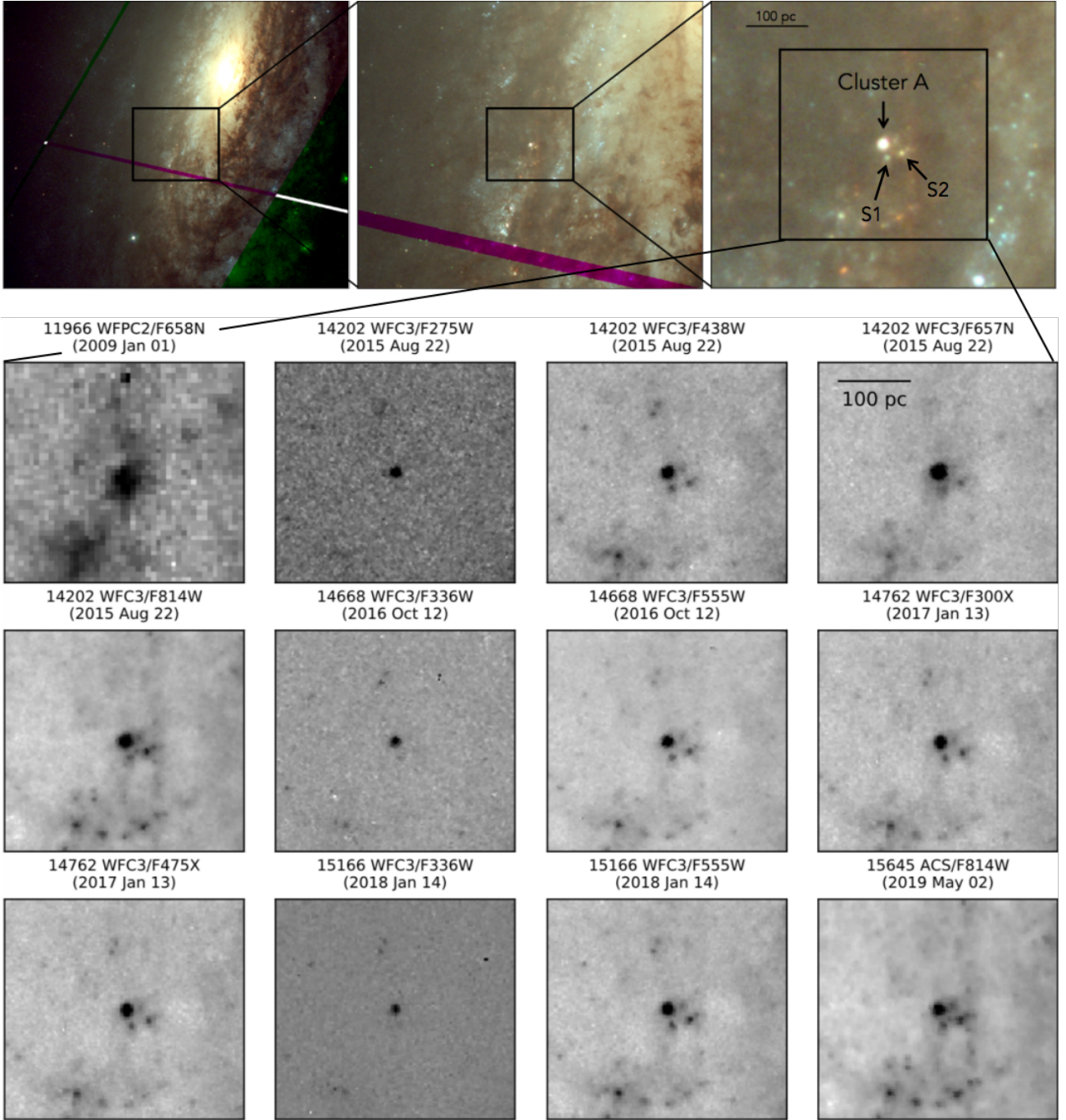


Figure 1. *HST* observations of the site of SN 2014C. The top panels are three-colour composite images of the F_{438W} (blue), F_{555W} (green) and F_{814W} (red) bands; the F_{438W} and F_{814W} images are from Program 14202 and the F_{555W} image is from Program 14668; the greenish and reddish regions are not covered by all three images. The other panels show the SN site from individual *HST* observations; the images are centred on *Cluster A* (i.e. SN 2014C’s host star cluster) and have been set to the same scale (the bar in the top-right panel corresponds to 100 pc). All panels are aligned such that North is up and East is to the left.

is now much cleaner, i.e., without significant contamination from its nearby sources.

4 PROPERTIES OF THE HOST STAR CLUSTER

We further try to infer the properties of *Cluster A* by fitting model spectra to its observed SED. Note that *Cluster A* is still associated with a considerable amount of (ionised) gas, given its bright emission in the F_{658N} band. The bright nebular line emission will significantly influence its broad-

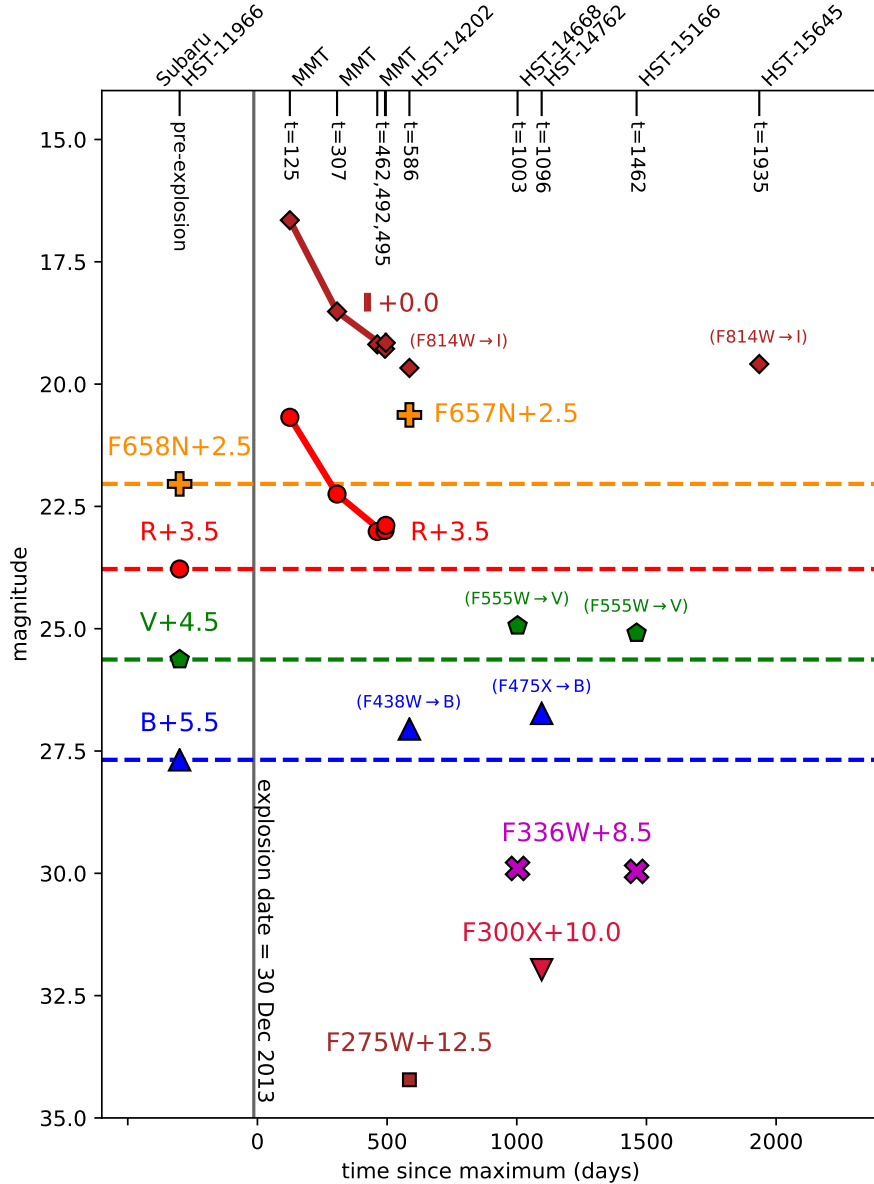


Figure 2. Magnitudes of *Cluster A* in different bands and at different epochs, when the light of SN 2014C may or may not be significant. Data points connected by solid lines are the late-time light curves of SN 2014C from M17. The horizontal dashed lines indicate the possible magnitudes of the host star cluster itself, i.e. without significant light contamination from SN 2014C.

band SED (e.g. $H\alpha$ in the R band) and must be modelled properly. To do this, we make use of the BPASS binary stellar population models (version 2.1; Eldridge, et al. 2017) to simulate the stellar component and the CLOUDY photoionisation code (version 17.01; Ferland, et al. 1998) to calculate the strength of nebular lines.

BPASS provides a large set of binary evolution models and spectral synthesis for stellar populations of various ages, metallicities and stellar initial mass functions. Binary evolution is calculated on a grid of initial mass ratio $M_2/M_1 = 0.1$ – 0.9 in steps of 0.1 , orbital period $\log(P/\text{days}) = 0.0$ – 4.0 in steps of 0.2 , and 68 values of primary stellar mass from 0.1 to $300 M_\odot$. While some binaries never interact during their lifetimes, some binaries do experience Roche-lobe overflow

(RLOF) or Common-Envelope (CE) evolution (the numerical recipe is described in Eldridge, Izzard & Tout 2008). Each population contains binaries with a flat distribution in the initial mass ratio and log-period. To accurately model *Cluster A*'s SED, it is very important to consider the effect of interacting binaries. Binary interaction can strip a star's envelope and prevent it from evolving into a cool RSG. As a result, the stripped star remains very hot and continues to provide ionising photons that power the nebular emission of the surrounding gas. As shown in a number of studies (e.g. Xiao, Stanway & Eldridge 2018; Xiao, et al. 2019), using population models without interacting binaries can significantly affect the estimate of physical properties.

Thus, we use the binary-star population models of

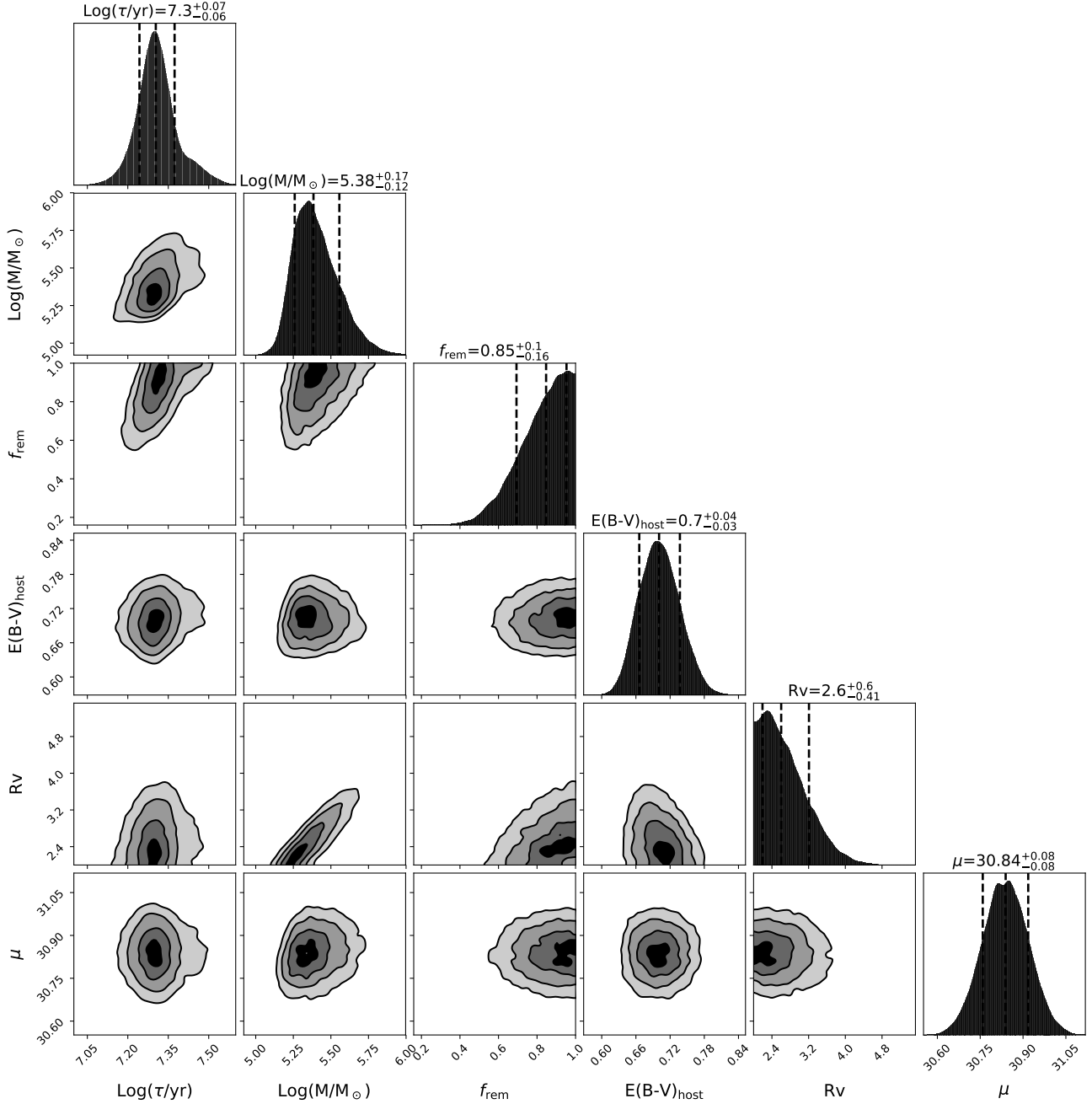


Figure 3. Marginalised posterior probability distributions over one (with median values and $1\text{-}\sigma$ credible intervals) and two dimensions (with 0.5, 1.0, 1.5 and $2.0\text{-}\sigma$ contours from inside to outside).

BPASS to model the stellar component of *Cluster A* while assuming a solar metallicity and a Kroupa (2001) initial mass function with a maximum stellar mass of $300 M_{\odot}$. Synthetic SEDs are then retrieved (from the file `spectra-bin-imf135_300.z020.dat.gz`) for stellar populations (which have been normalised to a total mass of $10^6 M_{\odot}$) as a function of age from $\log(\tau/\text{yr}) = 6.0$ to 11.0 in steps of 0.1 .

We then use CLOUDY to model the nebular emission with the BPASS SEDs as the ionising source. For simplicity, we firstly assume that the gas nebula is a spherical shell around the stars and that the nebula is dust-free, ionisation-

bound, and has a uniform, non-evolving density. We match the nebular metallicity with that of the stellar component and set the hydrogen density to be $\log(n_{\text{H}}/\text{cm}^{-3}) = 0.0$ to 5.0 in steps of 1.0 . This density range is consistent with the observed electron density for H II regions (e.g. Hunt & Hirashita 2009). The intensity of the ionising flux is characterised by the ionisation parameter:

$$U = \frac{Q(H)}{4\pi r_0^2 n_{\text{H}} c} \quad (1)$$

where $Q(H)$ is the hydrogen-ionising photon luminosity of

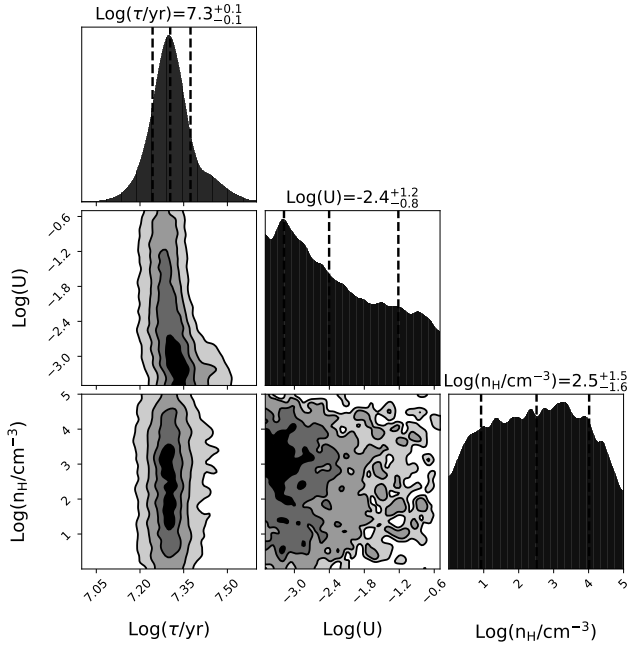


Figure 4. Same as Fig. 3 but for parameters of cluster age, ionisation parameter and hydrogen density.

the source, r_0 the inner radius of the nebula, and c is the speed of light. This parameter is the dimensionless ratio of hydrogen-ionising photon to hydrogen densities. We set $\log(U) = -3.5$ to -0.5 in steps of 0.3, which matches the observed range for H II regions (e.g. Rigby & Rieke 2004). For each combination of age, hydrogen density and ionisation parameter, we run the CLOUDY code to simulate the photoionisation process in the gas nebula. As an output, we obtain the synthetic spectrum for each model, which includes not only the emission from the stellar component but also that from the nebular component.

In practice, the ionising photons from massive stars may not all have a chance to interact with the surrounding gas. For example, the gas may not cover the full sky as viewed from the central stars. Alternatively, the gas shell may be optically thin and some ionising photons can escape without ionising any atoms. Thus, we use another parameter, f_{rem} , the fraction of remaining ionising photons that have not escaped, to characterise this “photon leakage effect” (Xiao, Stanway & Eldridge 2018; Xiao, et al. 2019). The value of f_{rem} can vary between 0 and 1, and the line fluxes are scaled linearly with f_{rem} to a good approximation.

We apply a Galactic reddening of $E(B-V)_{\text{mw}} = 0.08$ mag (Schlegel, Finkbeiner & Davis 1998) with a Galactic extinction law ($R_V = 3.1$; Fitzpatrick 2004). SN 2014C occurred in the dusty disk of its host galaxy (Fig. 1) and the interstellar reddening from its host galaxy is not negligible. Thus, we further redden the synthetic spectra by reddening values of $E(B-V)_{\text{host}} = 0.6$ to 1.0 in steps of 0.05. We assume a Fitzpatrick (2004) extinction law, but leave the total-to-selective extinction ratio $R_V = A_V/E(B-V)$ as a free parameter, ranging from 2.0 to 6.0 in steps of 0.5. A doppler shift, corresponding to *Cluster A*’s recession velocity (990 km s^{-1} ; Milisavljevic, et al. 2015), is applied to all the spectra. Syn-

thetic magnitudes for the spectra are calculated with the PYSYNPHOT package⁵.

We try to fit the observed SED of *Cluster A* with the synthetic ones. In doing this, we adopt a Gaussian prior for the distance modulus, μ , based on the reported distance of 14.7 ± 0.6 Mpc (i.e. $\mu = 30.84 \pm 0.04$). A Gaussian prior is also used for the host galaxy’s interstellar reddening based on the value derived by M15 from sodium absorption [$E(B-V)_{\text{host}} = 0.67$ mag], for which we assume a typical uncertainty of 0.05 mag. Flat priors are used for all the other parameters. Figures 3 and 4 display corner plots of the marginalised posterior probability distributions; a best-fitting spectrum is shown in Fig. 5.

The star cluster has a mass of $\log(M/M_\odot) = 5.38^{+0.17}_{-0.12}$ and an age of $\log(\tau/\text{yr}) = 7.30^{+0.07}_{-0.06}$ (i.e. $\tau = 20.0^{+3.5}_{-2.6}$ Myr). We derive a total-to-selective extinction ratio of $R_V = 2.6^{+0.6}_{-0.4}$, which seems to be smaller but still consistent with an average Galactic value of $R_V = 3.1$. The SED fitting suggests that $f_{\text{rem}} = 69\text{--}95\%$ of the ionising photons are interacting with the surrounding gas. Thus, the photon leakage effect is non-negligible despite the large uncertainty in f_{rem} . The ionisation parameter (U) and the hydrogen density (n_H) cannot be tightly constrained; detailed spectroscopic analysis is required to constrain these two parameters. However, they have very small effects on the determination of the star cluster’s age (e.g. Fig. 4).

M15 derived an age of 30–300 Myr by comparing the pre-explosion *BVR* photometry and $\text{H}\alpha$ luminosity with BPASS models. Our age estimate has a much smaller uncertainty since we have used more observations that were carried out in recent years. These observations cover a longer wavelength range from the ultraviolet *F275W* band to the near-infrared *F814W* band. Considering the possible contribution from ejecta-CSM interaction, we have very conservatively assume that all post-explosion observations can only provide upper limits for *Cluster A*’s brightness. Despite this, the upper limits are still very useful in constraining the cluster’s SED. For example, the UV upper limits exclude models that are too young and thus too UV-bright, and the *F814W* upper limits rule out old models with strong emission at long wavelengths. Moreover, the post-explosion observations are able to spatially resolve *Cluster A* and its nearby sources that are confused in the lower-resolution pre-explosion images. This allows us to decontaminate the *WFPC2/F658N* photometry and measure the $\text{H}\alpha$ emission of *Cluster A* more accurately (see Section 3 and Appendix B). $\text{H}\alpha$ is powered by the ionising photons from massive stars that ionise the surrounding gas. Thus, the bright $\text{H}\alpha$ emission also constrains *Cluster A* to have a young age.

5 PRE-SN EVOLUTION OF THE PROGENITOR SYSTEM

5.1 Summary of Observations

The age of *Cluster A* corresponds to the lifetime of SN 2014C’s progenitor and thus has important implications if the SN progenitor is coeval with its host star cluster. If we assume that the SN progenitor was a single star (or was

⁵ <https://pysynphot.readthedocs.io>

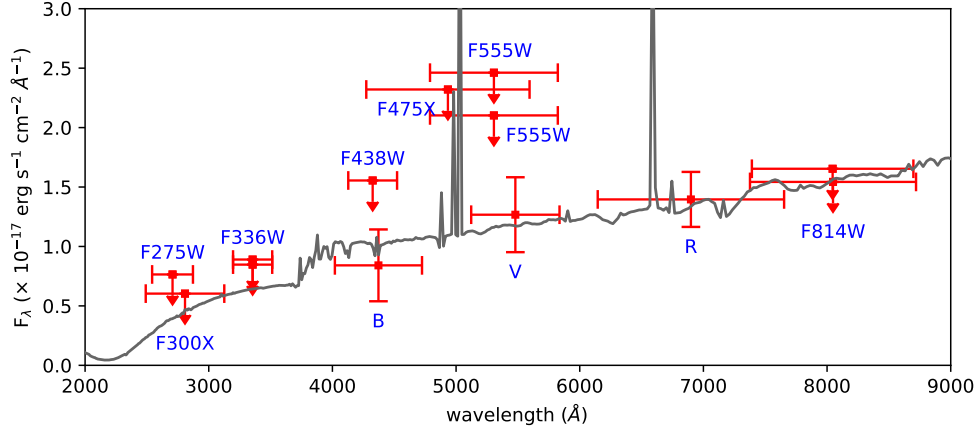


Figure 5. The observed SED (red data points) and best-fitting model spectrum (black line) of *Cluster A*. The data points are centred on the Pivot wavelength of each band, and the horizontal error bars represent the root-mean-square band widths of the filters. The vertical error bars reflect the $\pm 3\sigma$ photometric errors. Data points for the narrow bands are not displayed but they agree with the best-fitting model spectrum.

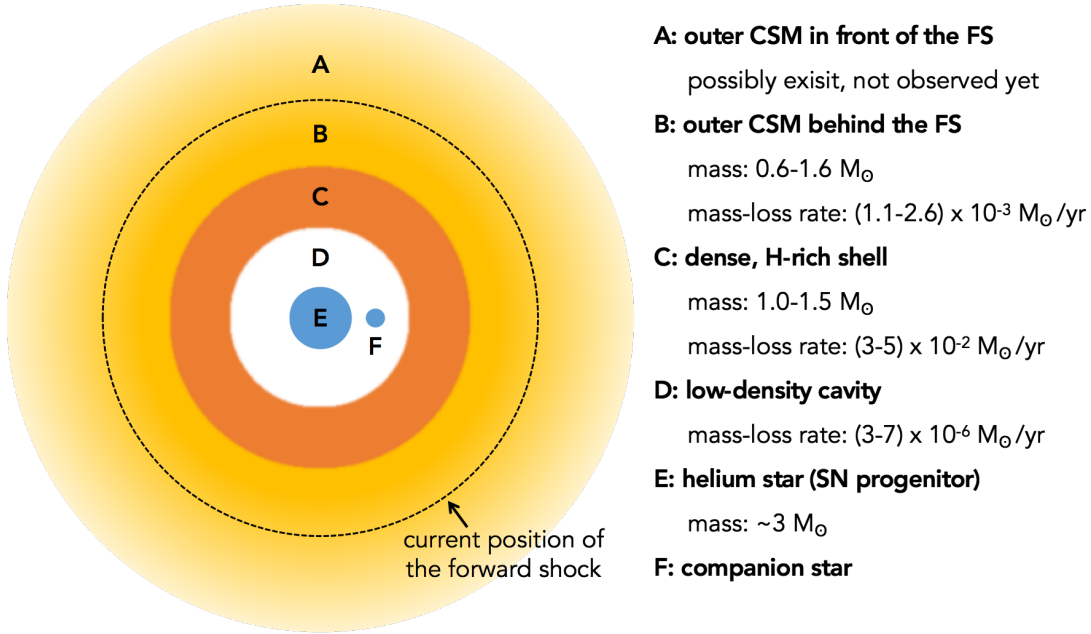


Figure 6. A schematic plot of SN 2014C's progenitor and its CSM (not to scale) just before core collapse. The dashed circle shows the forward shock (FS) position at the time of the most recent observations by T19 (1920.8 days post-maximum).

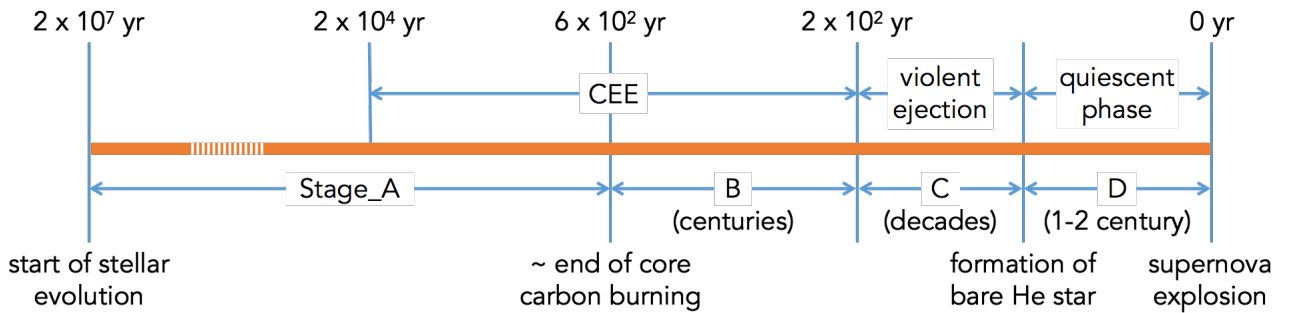


Figure 7. Timeline of the evolution of SN 2014C's progenitor, if its early-stage evolution follows that of Model *bpass1* or *bpass2*. At the top of the plot, the timescales correspond to the time before SN explosion.

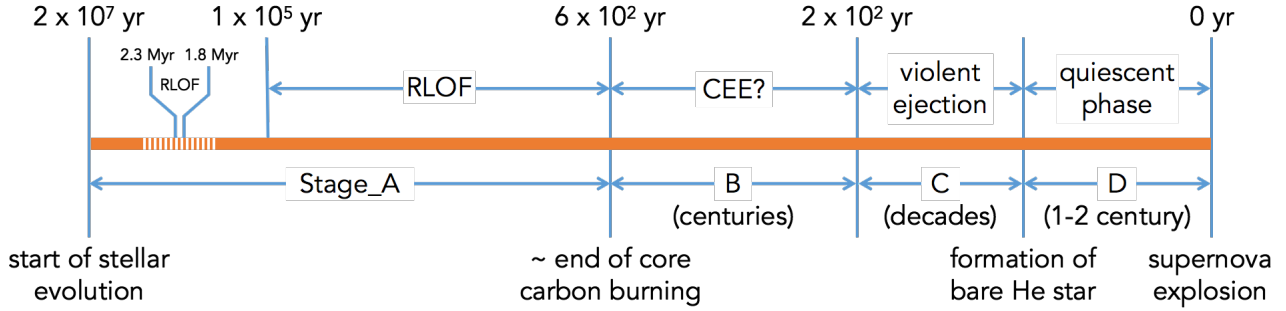


Figure 8. Same as Fig. 7, but if the early-stage evolution of SN 2014C’s progenitor follows that of Model *bpas3*.

in a non-interacting binary and “effectively single”), the lifetime of $\log(\tau/\text{yr}) = 7.30^{+0.07}_{-0.06}$ (i.e. $\tau = 20.0^{+3.5}_{-2.6}$ Myr) corresponds to an initial mass of $M_{\text{ini}} = 11.7^{+1.1}_{-1.0} M_{\odot}$ (according to the PARSEC v1.2S stellar evolutionary tracks; Bressan, et al. 2012). However, a single star of this initial mass should still retain a massive hydrogen envelope before it explodes as a hydrogen-rich Type IIP SN (Smartt 2009). This is inconsistent with SN 2014C; thus, the progenitor star must come from an interacting binary system. In this section we try to explore what kind of binary system can give rise to SN 2014C. To do this, it is important to summarise the observed properties of the progenitor star and the CSM (a schematic plot is shown in Fig. 6):

(1) The progenitor star has a lifetime of $\log(\tau/\text{yr}) = 7.30^{+0.07}_{-0.06}$ (i.e. $\tau = 20.0^{+3.5}_{-2.6}$ Myr; see Section 4).

(2) Since SN 2014C exhibited typical Type Ib spectra at early times, the hydrogen envelope of its progenitor star should be almost completely removed just before core collapse (a small amount of hydrogen may still be left as the near-maximum light spectrum shows an extended, high-velocity H α absorption feature; M15).

(3) By fitting to its bolometric light curve, M17 find that SN 2014C has a ^{56}Ni mass of $M_{\text{Ni}} = 0.15 \pm 0.02 M_{\odot}$, ejecta mass $M_{\text{ej}} = 1.7 \pm 0.2 M_{\odot}$, and explosion kinetic energy $E_{\text{k}} = (1.8 \pm 0.3) \times 10^{51}$ erg. The explosion parameters are very typical of Type Ib/c SNe (see e.g. Lyman, et al. 2016). In particular, the low ejecta mass suggests that the helium core of the progenitor star was only $M_{\text{He}} \sim 3 M_{\odot}$ if the compact remnant is a neutron star of $\sim 1.4 M_{\odot}$ (However, we caution that the derived ejecta mass may vary with the adopted opacity value in the light curve fitting; see, e.g., the discussion in Section 5.7 of Maund 2018).

(4) M17 did not detect any X-ray emission during the first ~ 20 days since the explosion of SN 2014C. The X-ray non-detection suggests that its progenitor star was located in a low-density cavity out to a distance of at least $(0.8-2) \times 10^{16}$ cm. The cavity corresponds to a low mass-loss rate of the progenitor system of $< (3-7) \times 10^{-6} M_{\odot} \text{ yr}^{-1}$ for a wind velocity of $v_{\text{w}} = 1000 \text{ km s}^{-1}$. Thus, the progenitor star did not suffer massive eruptions within $7(v_{\text{w}}/1000 \text{ km s}^{-1})$ years before core collapse. The ejecta-CSM interaction was very weak when the SN ejecta propagated through the low-density cavity; this is why SN 2014C did not exhibit any intermediate-width hydrogen lines at early times (M15).

(5) Outside the low-density cavity, there was a dense, hydrogen-rich CSM shell at a distance of 6×10^{16} cm with

a thickness of 10^{16} cm, a density of $2 \times 10^6 \text{ cm}^{-3}$, and a mass of $1-1.5 M_{\odot}$ (M17). Assuming an ejection velocity of 100 km s^{-1} (which is the upper velocity limit for the unshocked CSM; the unshocked gas is photoionised by the X-ray photons emitted by the shocked gas and thus can produce narrow emission lines; M15), the shell was formed ~ 190 years before core collapse and the mass-loss event lasted for ~ 30 years. Thus, the shell corresponds to a high mass-loss rate of the progenitor system of $(3-5) \times 10^{-2} M_{\odot} \text{ yr}^{-1}$, which is much higher than those of line-driven winds (Smith 2014). When the SN ejecta reached this shell at late times, the strong ejecta-CSM interaction produced prominent intermediate-width H α line emission, strong radio and X-ray radiation, and a slower decline rate in the light curve (as kinetic energy was converted into radiative energy; M15, M17, Anderson, et al. 2017, Bietenholz, et al. 2018).

(6) SN 2014C shows on-going ejecta-CSM interaction until 5 years post explosion (T19). Detailed light curve modelling suggests that there is an extended CSM component with a distinct density profile ($\rho \propto r^{-2}$) outside the dense shell. This outer CSM component reaches a distance of 2×10^{17} cm and has a mass of $0.6-1.6 M_{\odot}$. The inferred mass-loss rate is $(1.1-2.6) \times 10^{-3} M_{\odot} \text{ yr}^{-1}$, which is lower than that for the dense shell by an order of magnitude but still much higher than most line-driven winds (Smith 2014). Assuming an ejection velocity of 100 km s^{-1} , the mass-loss event that formed this outer CSM component started at least ~ 630 years before core collapse and lasted until the ejection of the dense shell. The density profile is typical for wind-driven mass loss; however, other types of mass loss can also generate the same density profile as long as the mass-loss rate is quasi-steady (e.g. Deschamps, et al. 2013, 2015). Following Fig. 6, we refer to this CSM component as *CSM_B*.

(7) The total mass of the progenitor star’s helium core and the CSM mentioned above is only $4.7-6.2 M_{\odot}$, which is smaller than the lower mass limit for a star that can undergo core collapse. This means that the progenitor star must have experienced significant mass loss at even earlier stages, during which it lost a considerable part of its hydrogen envelope. The stripped mass may have been accreted by a binary companion or have formed CSM located at further distances that have not yet been reached by the SN’s forward shock (thus, this CSM has not been excited to produce any observable features such as radio/X-ray emission and intermediate-width optical lines until the most recent ob-

servations by T19 at 1920.8 days post-maximum). We shall refer to this possible outmost CSM as *CSM_A*.

In summary, the progenitor star has experienced a complicated evolution with time-varying mass loss. Following the schematic plot of Fig. 6, we divide the progenitor star's pre-SN evolution into four stages (designated as *Stage_A* to *Stage_D*), during which the different CSM components were formed. Here *Stage_A* refers to the period from the beginning of stellar evolution until the onset of *Stage_B*. Since *CSM_B* were formed during the last few centuries of the progenitor, *Stage_A* lasted until approximately the end of core carbon burning (Woosley, Heger & Weaver 2002). Next we try to infer the progenitor system's evolution during the four stages. The timelines of two possible scenarios are provided in Figs. 7 and 8.

5.2 Stage_A

BPASS (Eldridge, et al. 2017) provides a grid of binary stellar evolution models spanning a wide range of parameters. The stellar evolution models are calculated until the end of core carbon burning, or neon ignition for the most massive stars. Thus, they are useful to investigate the *Stage_A* evolution of SN 2014C's progenitor system and we try to search for models with an end point meeting the following criteria:

(1) lifetime of the primary star is consistent with that of SN 2014C's host star cluster, i.e. $\log(\tau/\text{yr}) = 7.30^{+0.07}_{-0.06}$ (i.e. $\tau = 20.0^{+3.5}_{-2.6}$ Myr);

(2) the He core mass (M_{He}) is equal to that of the compact remnant (derived by BPASS for a typical SN explosion energy of 10^{51} erg) plus SN 2014C's ejecta mass of $1.7 \pm 0.2 M_{\odot}$ (M17);

(3) the primary star still has a residual hydrogen envelope with a mass of $M_{\text{env}} = 1.6\text{--}3.1 M_{\odot}$, which will be lost to form *CSM_B* (T19) and the dense shell at later stages (M15; Anderson, et al. 2017; M17).

Three models from BPASS can satisfy the above criteria, the parameters of which are listed in Table 3. All three models have a primary star with an initial mass of $11 M_{\odot}$. Models *bpass1* and *bpass2* have the same initial orbital period of $\log(P_{\text{ini}}/\text{days}) = 3.0$ and differ only in the initial secondary-to-primary mass ratio ($q_{\text{ini}} = 0.2$ for *bpass1* and $q_{\text{ini}} = 0.3$ for *bpass2*). Their evolution is also very similar. Figures 9 and 10 show the primary star's evolutionary track in the Hertzsprung–Russell diagram, the change in the primary star's mass and mass-loss rate, and the evolution of the orbital separation and period of the binary system. Models *bpass1* and *bpass2* both undergo *Case-C* mass transfer (i.e. the mass-donor star has already completed core helium burning when the mass transfer occurs) at very late times. The mass transfer is via CE ejection, starting from 2×10^4 years before the end of core carbon burning. The mass-loss rate reaches at most close to $\sim 10^{-3} M_{\odot} \text{ yr}^{-1}$ and several solar masses of the hydrogen envelope is removed until the end of the calculation.

Model *bpass3* has a larger initial secondary-to-primary mass ratio of $q_{\text{ini}} = 0.9$ and a shorter initial orbital period of $\log(P_{\text{ini}}/\text{days}) = 2.8$. Unlike Models *bpass1* and *bpass2*, Model *bpass3* undergoes *Case BC* mass transfer: the first episode of mass transfer occurs when the primary star is undergoing hydrogen shell burning while the second episode

starts when the star has finished core helium burning. Both mass-transfer episodes are via RLOF and are nearly conservative, i.e. all mass lost from the primary star is accreted by the secondary. However, the mass-loss rate is $< 10^{-4} M_{\odot} \text{ yr}^{-1}$ and much lower than those of models *bpass1* and *bpass2*.

5.3 Stage_B

5.3.1 Models *bpass1* and *bpass2*

It would be interesting to explore the further evolution of the progenitor system at later stages. For Models *bpass1* and *bpass2*, the mass-loss rate of the CE ejection at the end of core carbon burning $[(0.7\text{--}0.8) \times 10^{-3} M_{\odot} \text{ yr}^{-1}]$ is very close to that required for SN 2014C at *Stage_B* $[(1.1\text{--}2.6) \times 10^{-3} M_{\odot} \text{ yr}^{-1}; \text{T19}]$. Thus, it is very likely that the CE evolution continues to *Stage_B* after the end of core carbon burning. In other words, *CSM_A* and *CSM_B* in Fig. 6 are the CE that was ejected by the binary interaction. In the future, we may be able to see ongoing ejecta-CSM interaction as the forward shock propagates to further distances into the ejected material.

5.3.2 Model *bpass3*

For Model *bpass3*, the mass-loss rate for its second episode of mass transfer is only $6 \times 10^{-5} M_{\odot} \text{ yr}^{-1}$ at the end of core carbon burning. Moreover, the secondary star accretes almost all the material lost by the primary, leaving little to form a CSM (in this case, *CSM_A* in Fig. 6 may not exist at all). Thus, if SN 2014C's progenitor has followed the evolution of Model *bpass3*, we need some mechanism to increase the mass-loss rate by a factor of 20–40 and to form a dense CSM at *Stage_B*. For example, the envelope of RSGs may become dynamically unstable and develop large-amplitude pulsations (Yoon & Cantiello 2010); the fast envelope expansion may lead to a transition in the form of mass transfer from RLOF to CE evolution. However, more detailed modelling is needed to precisely understand the progenitor's late-time evolution.

5.4 Stage_C

Stage_B was followed by a violent mass ejection (i.e. *Stage_C*) in which $1\text{--}1.5 M_{\odot}$ of the last hydrogen layer (or 24–32% of the star's current mass) was lost within several decades to form the dense shell around SN 2014C (M15; M17). The mass-loss rate abruptly increased by an order of magnitude to $(3\text{--}5) \times 10^{-2} M_{\odot} \text{ yr}^{-1}$ and the ejected dense shell has a constant density profile, which is different from that of the outer CSM component (T19; see also the discussion in Section 5.1). This suggests that the mass loss at *Stage_C* may arise from a different mechanism from *Stage_B*. The mass-loss rate at *Stage_C* is comparable to those of LBV giant eruptions and the pre-SN eruptions of Type II_n/Ib_n SN progenitors (Smith 2017). Thus, *CSM_C* is likely to arise from a violent eruption from the progenitor star that occurred very close in time to core collapse.

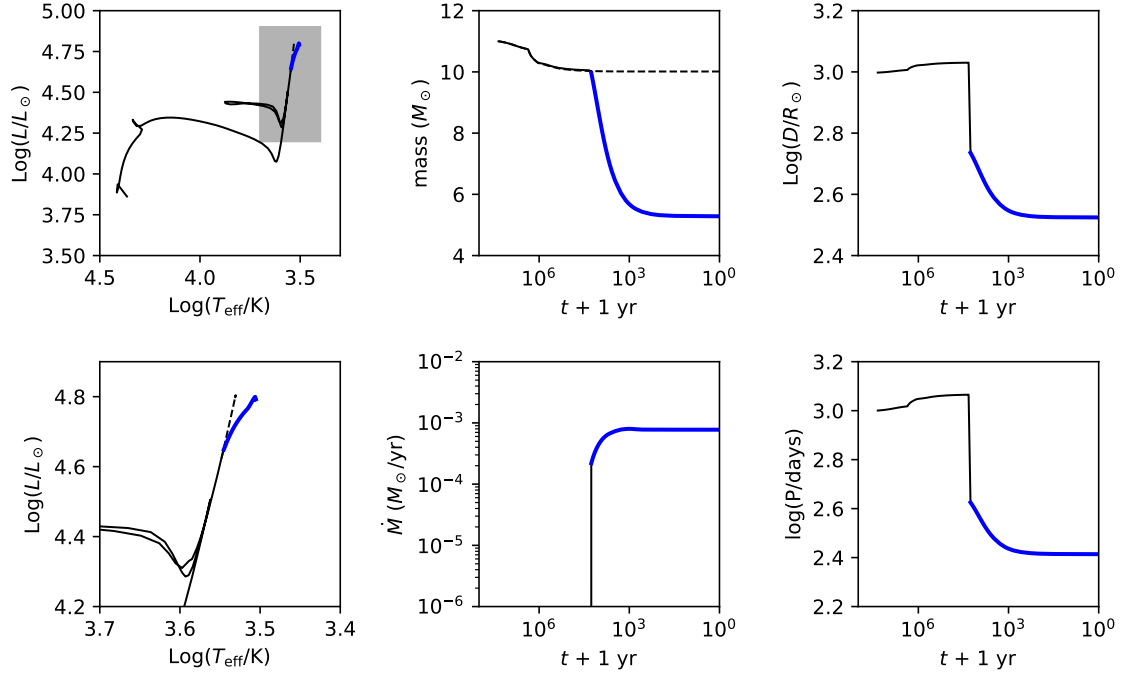


Figure 9. Model *bpas1*. The upper-left panel shows the primary star's evolutionary track in the Hertzsprung-Russell diagram, the grey-shaded part of which is zoomed and displayed in the lower-left panel. The middle panels show the evolution of the primary star's mass and mass-loss rate, and the right panels are the evolution of the binary system's orbital separation and period. In the middle and right panels, the horizontal axis corresponds to the time before the end of core carbon burning plus 1 year. The coloured, thick parts of the curves are when the mass transfer is happening between the binary stars. For comparison, the dashed lines correspond to a single star with the same initial mass of the primary star (i.e. $11 M_{\odot}$).

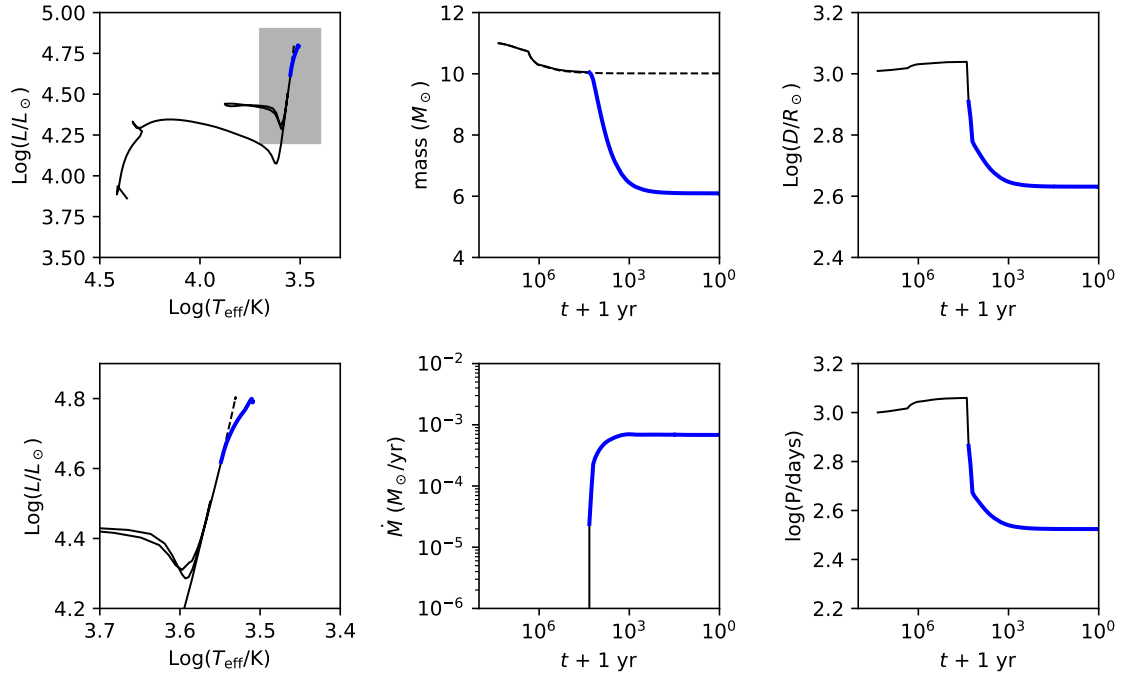


Figure 10. Same as Fig. 9 but for Model *bpas2*.

Table 3. BPASS models. Column 1: model ID. Columns 2–4: initial mass of the primary star, initial secondary-to-primary mass ratio, and initial orbital period. Column 5: lifetime of the primary star. Column 6: mass of the residual hydrogen envelope at the end of the simulation. Column 7: compact remnant mass of the primary star if it undergoes a SN explosion of typical explosion energy of 10^{51} erg. Column 8: helium core mass at the end of the simulation. Column 9: helium core mass minus the compact remnant mass, which should be the ejecta mass of SN 2014C (the residual hydrogen envelope was removed after the end of the simulation and just before core collapse).

model ID	$M_{\text{ini}}^1/M_{\odot}$	q_{ini}	$\log(P_{\text{ini}}/\text{days})$	$\log(\tau/\text{yr})$	M_{env}/M_{\odot}	M_{rem}/M_{\odot}	M_{He}/M_{\odot}	$(M_{\text{He}} - M_{\text{rem}})/M_{\odot}$
<i>bpass1</i>	11.0	0.2	3.0	7.35	2.02	1.46	3.26	1.80
<i>bpass2</i>	11.0	0.3	3.0	7.35	2.83	1.45	3.26	1.81
<i>bpass3</i>	11.0	0.9	2.8	7.35	1.83	1.45	3.15	1.70

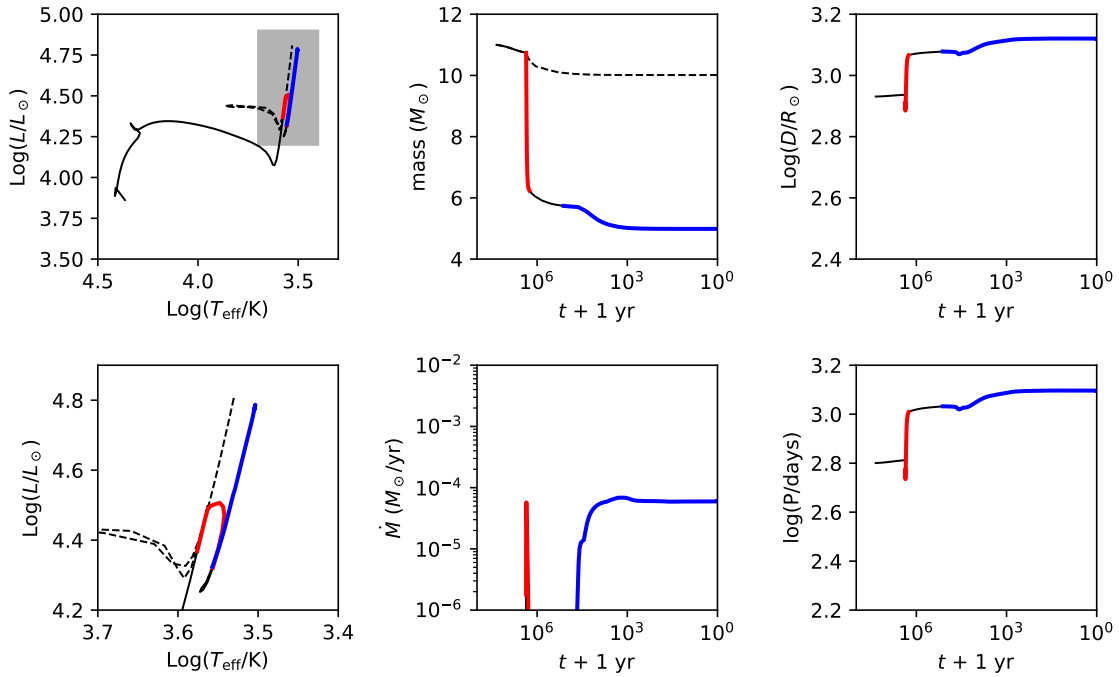


Figure 11. Same as Fig. 9 but for Model *bpass3*.

5.5 Stage_D

After the violent ejection at *Stage_C*, the progenitor star was almost a bare helium core of $\sim 3 M_{\odot}$ with very little hydrogen envelope. The low-density cavity around SN 2014C corresponds to a very low mass-loss rate $[< (3-7) \times 10^{-6} M_{\odot} \text{ yr}^{-1}]$; see the discussion of Section 5.1], suggesting that the progenitor remained quiescent in the final stage before its final explosion.

However, we cannot exclude the possibility that the progenitor was still subject to wind mass loss at this stage. For low-mass helium stars, the wind mass-loss prescription is still very uncertain, since very few such object have been identified from observations. By extrapolating the empirical prescription for WR stars (e.g. Nugis & Lamers 2000), Götzberg, et al. (2018) find a low mass-loss rate of $\log(\dot{M}/M_{\odot} \text{ yr}^{-1}) = -6.8$ for a helium star of $3.32 M_{\odot}$ at solar metallicity. The theoretical prescription of Vink (2017), however, predicts much weaker winds and that a $3 M_{\odot}$ helium star has a mass-loss rate of only $\log(\dot{M}/M_{\odot} \text{ yr}^{-1}) = -7.82$. Despite the large uncertainty, both predictions do not ex-

ceed the upper limit for SN 2014C's mass-loss rate inferred from its low-density cavity.

In summary, BPASS models suggest the progenitor of SN 2014C was an $11 M_{\odot}$ star in a relatively wide binary system that has experienced a complex mass-loss history (a schematic plot is shown in Fig. 12). Due to the relatively large initial orbital separation ($\sim 10^3 R_{\odot}$), the progenitor underwent a late episode of binary interaction very close to the end of its life. As a result, the ejected material formed an extended CSM component, which had not fully dissipated into the interstellar space when it was caught up by SN 2014C's ejecta. The binary interaction was only able to eject part of the hydrogen envelope before a violent eruption from the progenitor star ejected the remaining part. During the eruption, $1-1.5 M_{\odot}$ of the envelope was ejected within just several decades, which formed a dense shell of CSM around the progenitor system. After that, the progenitor star was almost a bare helium core and its mass loss was very weak, if any.

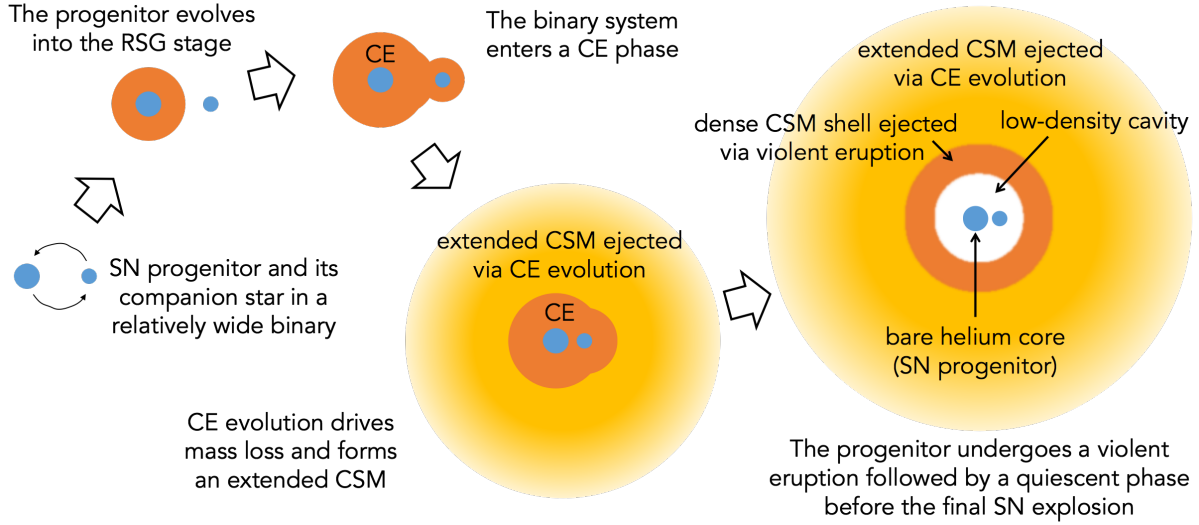


Figure 12. A schematic plot of SN 2014C’s progenitor system and its pre-SN evolution (based on Models *bpass1* and *bpass2*; for Model *bpass3*, the evolution is only slightly different; see text for details).

This quiescent phase lasted for only 1–2 centuries before the SN explosion and led to the formation of a low-density cavity between the progenitor and the dense CSM shell.

6 SUMMARY AND DISCUSSION

In this paper, we report a detailed analysis of the host star cluster of the transforming Type II_n/Ib_n SN 2014C. The analysis is based on *HST* observations, which cover a long wavelength range from the UV to the *F814W* band. The dataset also includes two narrow-band filters centred on the *Hα* and [N II] lines. We perform accurate photometry on the host star cluster and, when necessary, removed the contamination from nearby sources. We have reached the following conclusions:

(1) We find that the radiation from SN 2014C was still significant until at least 4 years after its explosion. This is consistent with the recent discovery that SN 2014C has an on-going interaction between the ejecta and extended CSM at far distances (T19). Still, photometry at post-explosion images provides important upper limits for the host star cluster’s brightness.

(2) We model the host star cluster’s SED with BPASS for the stellar population and CLOUDY for the gaseous nebula. The result suggests that it has an age of $\log(\tau/\text{yr}) = 7.30^{+0.07}_{-0.06}$ (i.e. $\tau = 20.0^{+3.5}_{-2.6}$ Myr) and a mass of $\log(M/M_{\odot}) = 5.38^{+0.17}_{-0.12}$. The age estimate rules out a single star progenitor for SN 2014C, assuming the progenitor to be coeval with the host star cluster. Thus, SN 2014C is most likely to arise from an interacting binary system.

(3) We further try to infer the initial configuration and the pre-SN evolution of the binary progenitor system. We find that three models from BPASS may be able to account for the early-stage evolution of the progenitor system. All are relatively wide binaries with an initial orbital period of $\log(P_{\text{ini}}/\text{days}) = 2.8\text{--}3.0$ and an initial mass of $11 M_{\odot}$ for the primary star. They underwent a *Case C* or *Case BC* mass transfer. In the former case, the mass transfer was via

CE evolution and the ejected CE formed the extended CSM outside the dense shell around SN 2014C.

(4) The progenitor star then experienced a violent eruption, in which $1.0\text{--}1.5 M_{\odot}$ of its last hydrogen layer was lost within decades to form a dense CSM shell. After the violent eruption, the progenitor star was almost a bare helium star, which stayed quite quiescent (although possibly still had a weak stellar wind) and ready for its final explosion.

Violent eruptions seem to be quite common for a significant number of (but not all) massive stars. The eruptions may be responsible for the dense CSM around Type II_n/Ib_n SNe and are sometimes directly observed as optical outbursts before the terminal SN explosion (e.g. SN 2006jc, Pastorello, et al. 2007; SN 2009ip, Mauerhan, et al. 2013; see also Ofek, et al. 2014). These phenomena suggest that the massive stars may become wildly unstable in the last centuries, decades, or even years before the end of their lives – something that has not been included in standard stellar evolutionary models.

Significant progress has been achieved in the past decade to understand the mechanism for the pre-SN eruptions of massive stars. For example, hydrodynamic waves may be excited by vigorous core convection at late nuclear burning stages; the waves, which propagate outward with a super-Eddington energy flux, can trigger an outburst of mass loss if they are able to reach close enough to the stellar surface (Quataert & Shiode 2012; Shiode & Quataert 2014; Fuller 2017; Fuller & Ro 2018). Moreover, the vigorous convection may cause finite-amplitude fluctuations in temperature, density, etc., and will be coupled non-linearly with nuclear burning. This may result in unsteady or even explosive nuclear burning that contribute to the mass ejection at late stages (Smith & Arnett 2014). Yet, more studies are still needed to fully understand the pre-SN eruptions.

It is also worth noting that SN 2014C’s dense shell corresponds to an extremely high mass-loss rate [$(3\text{--}5) \times 10^{-2} M_{\odot} \text{ yr}^{-1}$], which is similar to those of LBV giant eruptions. It was believed that such violent eruptions can only occur in stars which are initially more massive

than $25 M_{\odot}$. Recent observations, however, seem to suggest that eruptions with comparable intensities can also occur in lower-mass massive stars (a thorough discussion can be found in Section 6.3.2 of S20). In particular, Shivvers, et al. (2017) and S20 showed that the Type Ibn SNe 2006jc and 2015G may arise from lower-mass, interacting binary systems; yet, their progenitors underwent violent mass loss just before core collapse with similar characteristics of LBV giant eruptions (for SN 2006jc, the eruption was also observed as an optical outburst in 2004, two years before its final explosion; Pastorello, et al. 2007). This led S20 to conclude that lower-mass massive stars ($8 < M_{\text{ini}} < 25 M_{\odot}$) can also experience violent pre-SN eruptions that resemble LBV giant eruptions, if their envelopes are stripped in interacting binaries. The theoretical work of Fuller (2017) and Fuller & Ro (2018) also suggests that the removal of the envelope may aid the occurrence of pre-SN eruptions as in this case the convection-excited waves are easier to reach and trigger an outburst at the stellar surface.

SN 2014C may be the third example to support such a conclusion since its progenitor had an initial mass of only $\sim 11 M_{\odot}$ and was stripped by its companion. One difference from SNe 2006jc and 2015G is that, at the time of the eruption, SNe 2006jc's and 2015G's progenitors were almost bare helium stars while SN 2014C's progenitor was only partially stripped and still had a residual hydrogen envelope. This residual hydrogen envelope accounted for 24–32% of its total mass and was almost completely ejected within a few decades. Thus, the eruption was surprisingly violent for its mass and had a profound effect on the end product.

Another difference is also considerable between SN 2014C and other “normal” Type II_n/Ib_n SNe. For SN 2014C, the dense shell is located at a remote distance from the progenitor and its interaction with the SN ejecta started at very late times (~ 200 days after explosion; Anderson, et al. 2017). In contrast, many interacting SNe show strong ejecta-CSM interaction almost immediately after the SN explosion. This suggests that SN 2014C's dense shell was ejected a much longer time before the progenitor's core collapse than those of the “normal” Type II_n/Ib_n SNe. Such a difference may be related to different nuclear burning stages, stellar structures and/or energy sources for their mass loss. M17 studied a sample of Type Ib/c SNe and found that $\sim 10\%$ of them show a radio re-brightening at late times. Thus, it might be more common than previously thought for otherwise “normal” SNe to have CSM at remote distances just like SN 2014C. Many such SNe may have eluded our attention since they are not monitored continuously out to years or decades.

M17 also discussed the formation of SN 2014C's dense shell through a *Case C* binary interaction *or* through an eruption of its progenitor. In this paper, we find that both processes may have taken place, but they occurred at different evolutionary stages and were responsible for the formation of different CSM components. The ejected CE may be much more extended than the current position of the SN's forward shock. Thus, we predict that SN 2014C may remain bright in the next few years with enduring ejecta-CSM interaction.

In this paper we have assumed that the SN progenitor was the primary star in the system. Yet, we cannot exclude the possibility that the progenitor may be the initially sec-

ondary star with a compact companion (which was left after the primary star underwent core collapse). In this case, a merger between the two stars may also be able to eject the CE, trigger the violent mass ejection (Podsiadlowski, Morris & Ivanova 2006) and induce the subsequent SN explosion (Chevalier 2012). More detailed modelling is needed to fully and accurately understand the pre-SN evolution of SN 2014C's progenitor system.

ACKNOWLEDGEMENTS

We are grateful to the anonymous referee for his/her comments in improving this paper. N-CS acknowledges the funding support from the Science and Technology Facilities Council. This work is based on observations conducted with the Hubble Space Telescope and the data were retrieved from the data archive at the Space Telescope Science Institute. This work has also made use of the BPASS stellar population models.

DATA AVAILABILITY

The data used in this work are all publicly available from the Mikulski Archive for Space Telescope (<https://archive.stsci.edu>) and the Hubble Legacy Archive (<https://hla.stsci.edu>).

REFERENCES

- Anderson G. E., et al., 2017, MNRAS, 466, 3648
- Anupama G. C., Sahu D. K., Gurugubelli U. K., Prabhu T. P., Tominaga N., Tanaka M., Nomoto K., 2009, MNRAS, 392, 894
- Bestenlehner J. M., et al., 2014, A&A, 570, A38
- Bestenlehner J. M., 2020, MNRAS.tmp, doi:10.1093/mnras/staa474
- Bietenholz M. F., Kamble A., Margutti R., Milisavljevic D., Soderberg A., 2018, MNRAS, 475, 1756
- Bressan A., Marigo P., Girardi L., Salasnich B., Dal Cero C., Rubele S., Nanni A., 2012, MNRAS, 427, 127
- Bufano F., et al., 2009, ApJ, 700, 1456
- Cardelli J. A., Clayton G. C., Mathis J. S., 1989, ApJ, 345, 245
- Chevalier R. A., 2012, ApJL, 752, L2
- Chugai N. N., et al., 2004, MNRAS, 352, 1213
- Conti P. S., 1976., Mem. Soc. R. Sci. Liège, Liège, 9, 193
- Deschamps R., Siess L., Davis P. J., Jorissen A., 2013, A&A, 557, A40
- Deschamps R., Braun K., Jorissen A., Siess L., Baes M., Camps P., 2015, A&A, 577, A55
- Dolphin A. E., 2000, PASP, 112, 1383
- Eldridge J. J., Izzard R. G., Tout C. A., 2008, MNRAS, 384, 1109
- Eldridge J. J., et al., 2017, PASA, 34, e058
- Elson R. A. W., Fall S. M., Freeman K. C., 1987, ApJ, 323, 54
- Ferland G. J., Korista K. T., Verner D. A., Ferguson J. W., Kingdon J. B., Verner E. M., 1998, PASP, 110, 761
- Fesen R. A., et al., 1999, AJ, 117, 725
- Fitzpatrick E. L., 2004, ASPC, 33, ASPC..309
- Foley R. J., Smith N., Ganeshalingam M., Li W., Chornock R., Filippenko A. V., 2007, ApJL, 657, L105
- Fransson C., et al., 2005, ApJ, 622, 991
- Freedman W. L., et al., 2001, ApJ, 553, 47
- Fuller J., 2017, MNRAS, 470, 1642
- Fuller J., Ro S., 2018, MNRAS, 476, 1853

- Gal-Yam A., et al., 2007, *ApJ*, 656, 372
- Gal-Yam A., Leonard D. C., 2009, *Natur*, 458, 865
- Gennaro M., et al., 2018, *WFC3 Data Handbook*, Version 4.0, (Baltimore: STScI)
- Georgy C., et al., 2012, *A&A*, 542, A29
- Götberg Y., de Mink S. E., Groh J. H., Kupfer T., Crowther P. A., Zapartas E., Renzo M., 2018, *A&A*, 615, A78
- Groh J. H., Meynet G., Ekström S., 2013, *A&A*, 550, L7
- Groh J. H., Meynet G., Georgy C., Ekström S., 2013, *A&A*, 558, A131
- Harris W. E., 2018, *AJ*, 156, 296
- Hosseinzadeh G., et al., 2017, *ApJ*, 836, 158
- Humphreys R. M., Davidson K., Smith N., 1999, *PASP*, 111, 1124
- Hunt L. K., Hirashita H., 2009, *A&A*, 507, 1327
- Immler S., et al., 2008, *ApJL*, 674, L85
- Jordi K., Grebel E. K., Ammon K., 2006, *A&A*, 460, 339
- Kroupa P., 2001, *MNRAS*, 322, 231
- Lucas R. A., et al., 2018, *ACS Data Handbook*, Version 9.0 (Baltimore: STScI).
- Lyman J. D., Bersier D., James P. A., Mazzali P. A., Eldridge J. J., Fraser M., Pian E., 2016, *MNRAS*, 457, 328
- Margutti R., et al., 2017, *ApJ*, 835, 140 (M17)
- Massey P., 2003, *ARA&A*, 41, 15
- Mauerhan J. C., et al., 2013, *MNRAS*, 430, 1801
- Maund J. R., 2018, *MNRAS*, 476, 2629
- Milisavljevic D., et al., 2015, *ApJ*, 815, 120 (M15)
- Miyazaki S., et al., 2002, *PASJ*, 54, 833
- Nugis T., Lamers H. J. G. L. M., 2000, *A&A*, 360, 227
- Ofek E. O., et al., 2014, *ApJ*, 789, 104
- Osterbrock D. E., 1989, *Astrophysics of Gaseous Nebulae and Active Galactic Nuclei*, University Science Books, Sausalito, CA
- Pastorello A., et al., 2007, *Natur*, 447, 829
- Pastorello A., et al., 2008, *MNRAS*, 389, 113
- Peng C. Y., Ho L. C., Impey C. D., Rix H.-W., 2002, *AJ*, 124, 266
- Peng C. Y., Ho L. C., Impey C. D., Rix H.-W., 2010, *AJ*, 139, 2097
- Podsiadlowski P., Morris T. S., Ivanova N., 2006, in Kraus M., Miroshnichenko A. S., eds, *ASP Conf. Ser. Vol. 35, Stars with the B[e] Phenomenon*. Astron. Soc. Pac., San Francisco, p. 259
- Quataert E., Shiode J., 2012, *MNRAS*, 423, L92
- Rigby J. R., Rieke G. H., 2004, *ApJ*, 606, 237
- Schlegel D. J., Finkbeiner D. P., Davis M., 1998, *ApJ*, 500, 525
- Shiode J. H., Quataert E., 2014, *ApJ*, 780, 96
- Shivvers L., et al., 2017, *MNRAS*, 471, 4381
- Sirianni M., et al., 2005, *PASP*, 117, 1049
- Smartt S. J., 2009, *ARA&A*, 47, 63
- Smith N., Hartigan P., 2006, *ApJ*, 638, 1045
- Smith N., Frew D. J., 2011, *MNRAS*, 415, 2009
- Smith N., 2014, *ARA&A*, 52, 487
- Smith N., Arnett W. D., 2014, *ApJ*, 785, 82
- Smith N., 2017, *Handbook of Supernovae*. Springer International Publishing AG, Cham, p. 403
- Smith N., et al., 2017, *MNRAS*, 466, 3021
- Smith N., Aghakhanloo M., Murphy J. W., Drout M. R., Stassun K. G., Groh J. H., 2019, *MNRAS*, 488, 1760
- Sun N.-C., et al., 2017, *ApJ*, 835, 171
- Sun N.-C., et al., 2017, *ApJ*, 849, 149
- Sun N.-C., et al., 2018, *ApJ*, 858, 31
- Sun N.-C., Maund J. R., Hirai R., Crowther P. A., Podsiadlowski P., 2020, *MNRAS*, 491, 6000 (S20)
- Tinyanont S., et al., 2019, *ApJ*, 887, 75 (T19)
- Vink J. S., 2012, *Eta Carinae and the Supernova Impostors*, Springer Science+Business Media, p. 221
- Vink J. S., 2017, *A&A*, 607, L8
- Woosley S. E., Heger A., Weaver T. A., 2002, *RvMP*, 74, 1015
- Xiao L., Stanway E. R., Eldridge J. J., 2018, *MNRAS*, 477, 904
- Xiao L., Galbany L., Eldridge J. J., Stanway E. R., 2019, *MNRAS*, 482, 384
- Yoon S.-C., Cantiello M., 2010, *ApJL*, 717, L62

APPENDIX A: PHOTOMETRY WITH GALFIT

It is not trivial to perform photometry on unresolved star clusters that are more extended than point sources, especially when they are in crowded regions. Aperture photometry with a large aperture radius will unavoidably include the contamination from nearby sources. Alternatively, if one uses a small aperture radius, it is necessary to perform aperture correction to compensate for the light outside the aperture radius. However, the aperture correction for an extended source may be different from that derived from stars. To overcome these difficulties, we use the GALFIT package (Peng, et al. 2002, 2010) to model the *HST* images of *Cluster A* and its nearby sources (within $1.6'' \times 1.6''$ box regions centred on *Cluster A* and aligned with the image axes; Figs. A1, A2). In this way, the star cluster and its nearby sources can be isolated and their magnitudes can be derived accurately from model fitting. Model PSFs, generated with the TinyTim package, are used in GALFIT.

For the *F658N* band, *Cluster A* falls on the *WF3* chip of *WFPC2*, which has a poorer spatial resolution compared with the other images taken by *WFC3/UVIS* and *ACS/WFC*. As a result, the emission from *Cluster A*, *S1* and *S2* cannot be spatially resolved and appears to be a single, extended source. Thus, we model the image with a single Gaussian profile plus a flat sky background.

The *F657N*-band image has a higher spatial resolution and reveals *S1* and *S2* in the vicinity of *Cluster A*; we use a Gaussian profile to model each of them. For *Cluster A*, however, we find that a single Gaussian profile does not reproduce its light distribution; instead, it is better described by the sum of two Gaussian profiles with different FWHMs. A flat sky background is also included.

In the broad-band images, the light of *Cluster A* comes mainly from its stellar component. We model the star cluster with a Moffat profile

$$\Sigma(r) \propto \frac{1}{[1 + (r/r_c)^2]^{\gamma/2}} \quad (\text{A1})$$

where Σ is the surface brightness, R the projected distance to the cluster centre, and r_c the core radius. This profile has a flat core near the centre with a power-law decline at larger radius and can well describe the light profile of young star clusters (Elson, Fall & Freeman 1987). For the nearby stars in the field, we first run the DOLPHOT package (Dolphin 2000) to get a stellar catalogue with positions and magnitudes; each star is then modelled with a narrow Gaussian function with a position and magnitude as derived by DOLPHOT and a FWHM of 0.5 pixel (which is equivalently a delta function). For the brightest three stars in each image, we allow their positions, magnitudes, and FWHMs to be adjusted during the fitting. This is because the stars may not be perfect PSFs as they may be confused by other nearby stars or may even be unresolved star clusters. For all the other stars their model parameters are fixed to save computing power. A flat sky background is included.

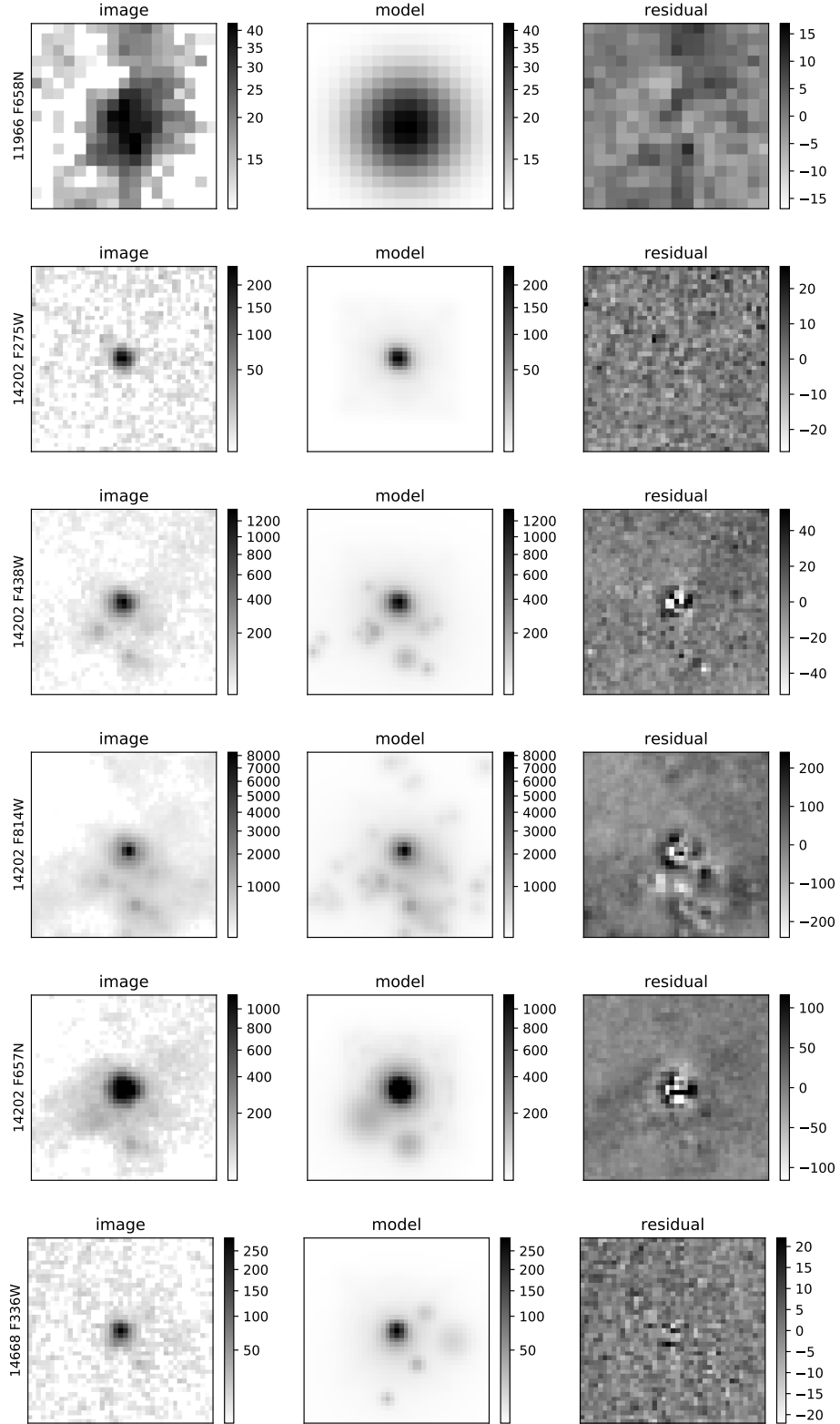


Figure A1. Images, models, and the residuals of the star cluster region. The colour bars are in units of analog-to-digital units. The images are centred on *Cluster A* and aligned with the image axes. Each set of image is labeled with its *HST* program ID and its filter (see Table 1).

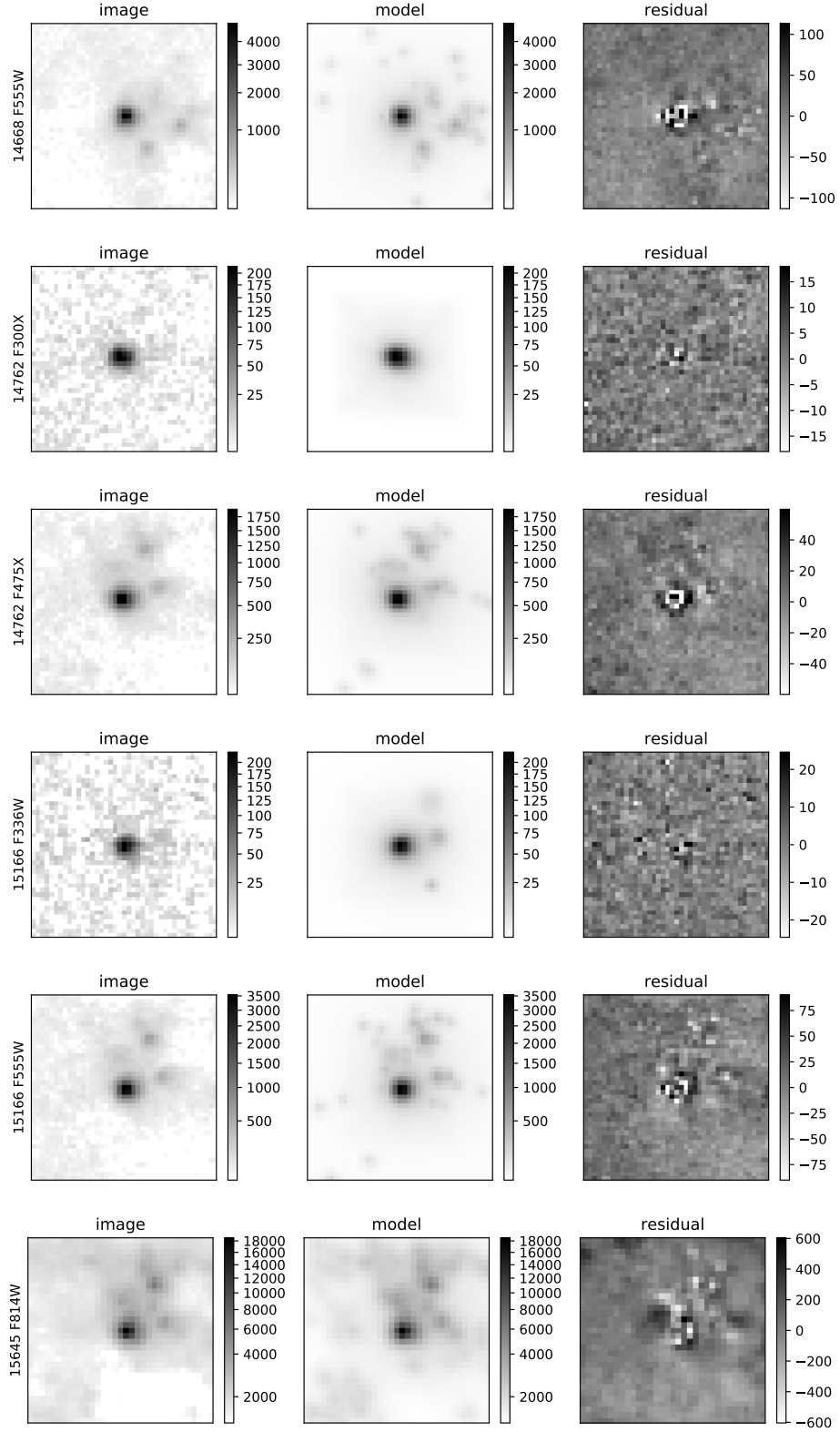


Figure A2. Continued

The broad-band images can be fitted well with the above models, except for the *F814W* band, where large residuals exist at the positions of field stars. The number of field stars are the most numerous in the *F814W*-band images and, as a result, source crowding and confusion is most severe in these images. With a few tests, we find that they can be modelled best if we use larger FWHMs in the Gaussian profiles for the field stars (1.0 pixel for the *F814W*-band image of Program 14202 and 1.5 pixel for that of Program 15645). This effectively uses a wider profile than the PSF to model the stars to better account for source crowding and confusion.

The observed, model and residual images of all bands are displayed in Figs. A1 and A2. The residuals are all on very small levels compared with the significant brightness of the star cluster. We also have calculated the total residual fluxes within 5 pixels from the cluster centre, which are then added to *Cluster A*'s model fluxes in the corresponding bands. The residual fluxes, however, are all smaller than the fitting uncertainties.

APPENDIX B: DECONTAMINATION OF *WFPC2/F658N* PHOTOMETRY

Due to the poor spatial resolution, the source in the *WFPC2/F658N* image includes the contribution not only from *Cluster A* but also from *S1* and *S2* in its close proximity. To study the properties of *Cluster A*, we must estimate and remove the contribution of *S1* and *S2* properly.

To this end, we first linearly interpolate the continuum fluxes of *S1* and *S2* in the *WFC3/F657N* and *WFPC2/F658N* bands from their *F555W*- and *F814W*-band fluxes [$F555W(S1) = 23.67 \pm 0.03$ mag; $F814W(S1) = 22.07 \pm 0.01$ mag; $F555W(S2) = 23.42 \pm 0.02$ mag; $F814W(S2) = 21.68 \pm 0.01$ mag]. We then create synthetic spectrum by adding emission lines of $H\alpha$ and $[N\ II]\ \lambda\lambda 6548, 6584$ to the continuum; the line wavelengths have been Doppler-shifted with a recession velocity of 990 km s^{-1} (M15) and we assume the flux ratio of $([N\ II]\ \lambda 6548)/([N\ II]\ \lambda 6584)$ to be 1/3 (Osterbrock 1989). We adjust the fluxes of $H\alpha$ and $[N\ II]$ lines until the synthetic magnitudes of *S1* and *S2* in the *WFC3/F657N* band match those derived from GALFIT within errors [$F657N(S1) = 21.61 \pm 0.06$ mag; $F657N(S2) = 20.85 \pm 0.04$ mag]. The brightness of *S1* and *S2* in the *WFPC2/F658N* band can then be estimated with their synthetic magnitudes.

We find that the results are weakly dependent on the flux ratio of $([N\ II]\ \lambda 6584)/(H\alpha\ \lambda 6563)$. By changing this ratio from 0.01 to 1.0, the *WFPC2/F658N*-band magnitude varies over a range of 19.70–19.83 mag for *S1* and 20.74–20.874 mag for *S2*. As a result, *Cluster A*'s contribution lies within 19.47–19.62 mag. We take the median value (19.54 mag) as the decontaminated magnitude of *Cluster A* and the half range (0.07 mag) as the uncertainty caused by the unknown $([N\ II]\ \lambda 6584)/(H\alpha\ \lambda 6563)$ flux ratio. This uncertainty is combined with the model fitting error as the total uncertainty. Thus, we obtain the decontaminated magnitude of *Cluster A* as $F658N = 19.54 \pm 0.09$ mag.

This paper has been typeset from a \LaTeX file prepared by the author.